Cavitation effect of holmium laser pulse applied to ablation of hard tissue underwater

Tao Lü
Huazhong University of Science and Technology
College of Optoelectronics Science and Engineering
Wuhan National Laboratory for Optoelectronics
Wuhan, China 430074
and
China University of Geosciences
School of Mathematics and Physics
Wuhan, China 430074

Qing Xiao
Huazhong University of Science and Technology
Britton Chance Center for Biomedical Photonics
Wuhan National Laboratory for Optoelectrics
Wuhan, China 430074

Danqing Xia
Kai Ruan
Zhengjia Li
Huazhong University of Science and Technology
College of Optoelectrics Science and Engineering
Wuhan National Laboratory for Optoelectronics
Wuhan, Hubei, 430074 China

Abstract. To overcome the inconsecutive drawback of shadow and schlieren photography, the complete dynamics of cavitation bubble oscillation or ablation products induced by a single holmium laser pulse [2.12 μm, 300 μs (FWHM)] transmitted in different core diameter (200, 400, and 600 μm) fibers is recorded by means of high-speed photography. Consecutive images from high-speed cameras can stand for the true and complete process of laser-water or laser-tissue interaction. Both laser pulse energy and fiber diameter determine cavitation bubble size, which further determines acoustic transient amplitudes. Based on the pictures taken by high-speed camera and scanned by an optical coherent microscopy (OCM) system, it is easily seen that the liquid layer at the distal end of the fiber plays an important role during the process of laser-tissue interaction, which can increase ablation efficiency, decrease heat side effects, and reduce cost. © *2010 Society of Photo-Optical Instrumentation Engineers.*
[DOI: 10.1117/1.3470092]

Keywords: holmium laser pulse; cavitation bubble; acoustic transient; laser-tissue interaction; optical coherent microscopy system.

Paper 10237R received May 3, 2010; revised manuscript received May 31, 2010; accepted for publication Jun. 2, 2010; published online Aug. 5, 2010.

1 Introduction

Pulsed holmium lasers with wavelengths of 2.12 μm are studied today for a wide range of medical applications. Due to their strong absorption in water (absorption coefficient $\sim$30 cm^{-1}) and excellent transmission in low OH$^-$ quartz fibers, they are a very useful tool for the precise ablation of biological tissues with low thermal damage.[1,2] In several medical applications, the procedure is performed in a liquid environment, for example, in arthroscopic surgery[3] and in orthopedic procedures.[4] When the optical fiber is not in direct contact with tissue, a cavitation bubble (CB) is formed by absorption of laser radiation in the liquid separating the fiber tip and the tissue surface.[1–5] A CB undergoes many expansions, collapses, shock wave emissions,[6,7] and liquid jets,[8,9] which can lead to mechanical tissue damage and/or destruction of the delivery instrument. An additional complication of endoscopic orthopedic procedures is that the freedom of movement in the joint is limited to a few millimeters, and the tissue surface that has to be irradiated is often not in an axial direction to the fiber applicator.[2] Consequently, in practice, some liquid always exists in the space between the fiber tip and the tissue surface, even if the fiber tip is in contact with the tissue surface. Water thermodynamics can be an essential contributor to the overall mechanisms of laser-tissue interaction.[10]

However, much literature reported not a sequential but a transient phase of CBs and ablation products by performing shadow and schlieren photography.[1,6,7,11–15] All presented images must be reconstructed from different CBs and ablation products induced by laser pulses with theoretically identical parameters, but during different laser-liquid interaction processes.[1] These images do not stand for the true dynamics of CBs and ablation products because: 1. pulse width and pulse energy are always fluctuant in actual circumstances;[9] and 2. the more serious drawback is that the response time of a holmium laser apparatus is variable because of the inherent problems of the power circuits, even under the same ambient circumstance. As a result, the accuracies of the presented images are suspicious. In our prior study, this phenomenon is observed and verified. However, high-speed photography[8,9,16–19] can overcome the drawbacks of shadow and schlieren photography due to a complete process that can be recored accurately under the same condition.

The main goal of this study was to visualize a complete dynamcis of CBs or ablation products induced by a single holmium laser pulse transmitted in different core diameter (200, 400, and 600 μm) fibers. High-speed photography and acoustic pressure sensor were applied to record and detect the dynamics of CBs or ablation products, and acoustic transients, respectively. Unlike conventional optical coherent tomograph (OCT) systems, optical coherent microscopy (OCM) systems are applied to measure the surface and internal morphology, and ablation rate for hard tissues (calculus) more precisely, which could contribute to evaluate the difference of ablation ability of holmium laser pulses in air and in a liquid environ-

Address all correspondence to: Zhengjia Li, Huazhong University of Science and Technology, College of Optoelectronics Science and Engineering, Wuhan, Hubei, 430074, China. Tel: 86-278-779-3019. E-mail: zhjli@mail.hust.edu.cn

1083-3668/2010/15(4)/048002/9/$25.00 © 2010 SPIE

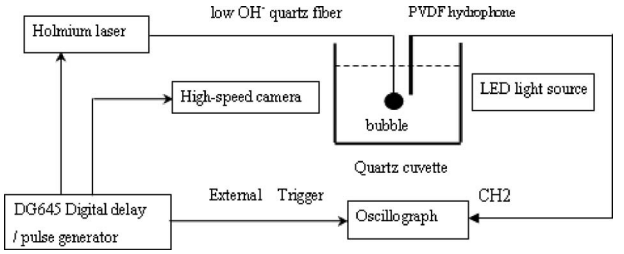

Fig. 1 Schematic diagram of the experimental setup.

ment. Consequently, the role of the liquid layer for ablating hard tissue could be much more clear.

2 Materials and Methods

2.1 *Experimental System*

A schematic diagram of the experimental setup is shown in Fig. 1. The used free-running Ho:YAG laser apparatus (Wuhan National Laboratory for Optoelectronics) can emit lasers with pulse durations of 300 μs [full width at half-maximum (FWHM)], wavelengths of 2.12 μm, a pulse energy of up to more than 2 J, and a repetition rate of up to 40 Hz. Here, the laser energy can be coupled into low OH^- quartz fibers (length 2 m) with different core/cladding diameters (200/240 μm, 400/440 μm, and 600/660 μm, NA=0.22) by a C_aF_2 lens (diameter 20 mm, focal length 50 mm), respectively. The distal fiber tips are all positioned in a quartz cuvette (diamensions $10\times10\times10$ cm^3) filled with pure water (drinking water) at room temperature. The fiber tips are kept at least 3 cm below the water surface to insure sufficient inertial confinement. AB, CD, and EF channels of the front pannel of a DG645 digital delay/pulse generator (Standford Research System, Sunnyvale, California) are linked with holmium laser apparatus, high-speed camera (Fastcam SA1.1, Japan, maximum frame rate of 675,000 frames per second, spatial resolution of 64×16 pixels), and oscillograph [Agilent Technologies (Santa Clara, California) InfiniVision, 350 MHz, 2 GSa/s] via BNC connectors, respectively. The pulse widths and the voltage amplitudes of the three channels are all 100 ns and 5 V, respectively. Only after the LED light source is initiated can DG645 perform with a mode of single-shot triggering. As a result, bubble dynamics and shock waves are recorded and detected by the camera and the piezoelectric polyvinylidenefluoride (PVDF) needle hydrophone (Institute of Acoustics, Chinese Academy of Sciences, sensitivity of more than 10 nV/Pa, response time of about several tens of nanoseconds, and an active zone diameter of 0.8 mm), respectively.

The spatial beam profile of the free-running Ho:YAG laser consists of several modes. Consequently, high-order fiber modes are excited, resulting in an inhomogeneous power distribution at the distal surface of the fiber. A typical power distribution and temporal pulse shape of holmium lasers are shown in Fig. 2.

2.2 *Hard Tissue Treatment*

To study the dynamcis of ablation products induced by holmium laser pulse, some calculus as hard tissue was applied in our experiments. Calculus consisting of calcium oxalate monohydrate (COM) and uric acid (UC) constituents with a planar surface was extracted from a 22-year-old female patient from Tongji Hospital of Tongji Medical College of Huazhong University of Science and Technology. Analysis of the calculus constituents was important for the fragmentation process. To make the pellets, we ground KB_r and a sample together into a powder with a mortar and pestle. The powder was then loaded into a press cell. A pellet was formed by

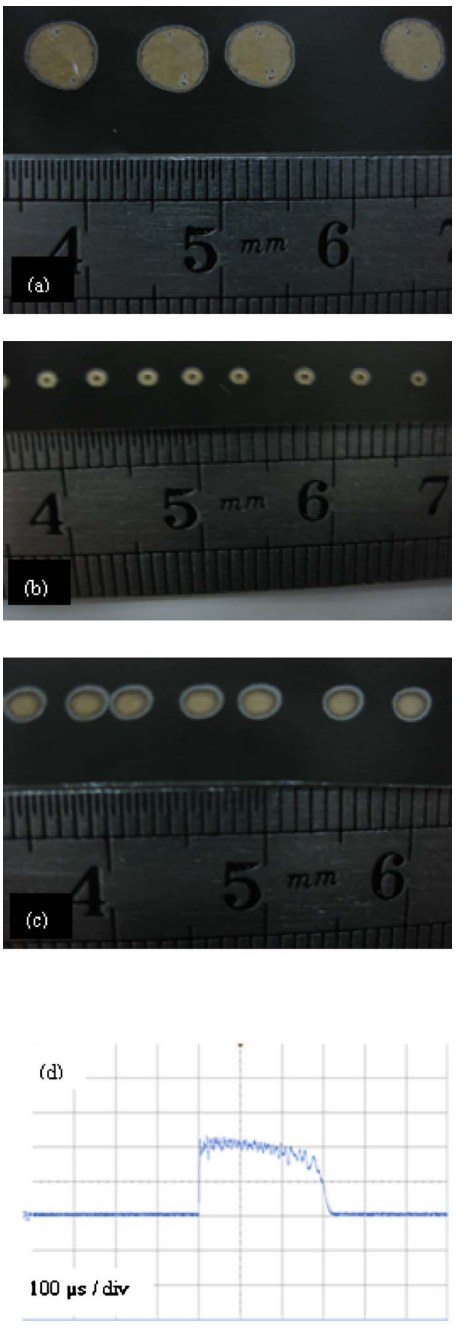

Fig. 2 2-D thermal images of the holmium laser power distribution at the distal fiber surface at various distances from black photograph paper with a repetition rate of 5 Hz. (a) Without fiber coupler, (b) with fiber coupler and a distance of 1 mm, (c) with fiber coupler and a distance of 3 mm, and (d) temporal pulse shape of holmium laser pulse [300 μs (FWHM)].

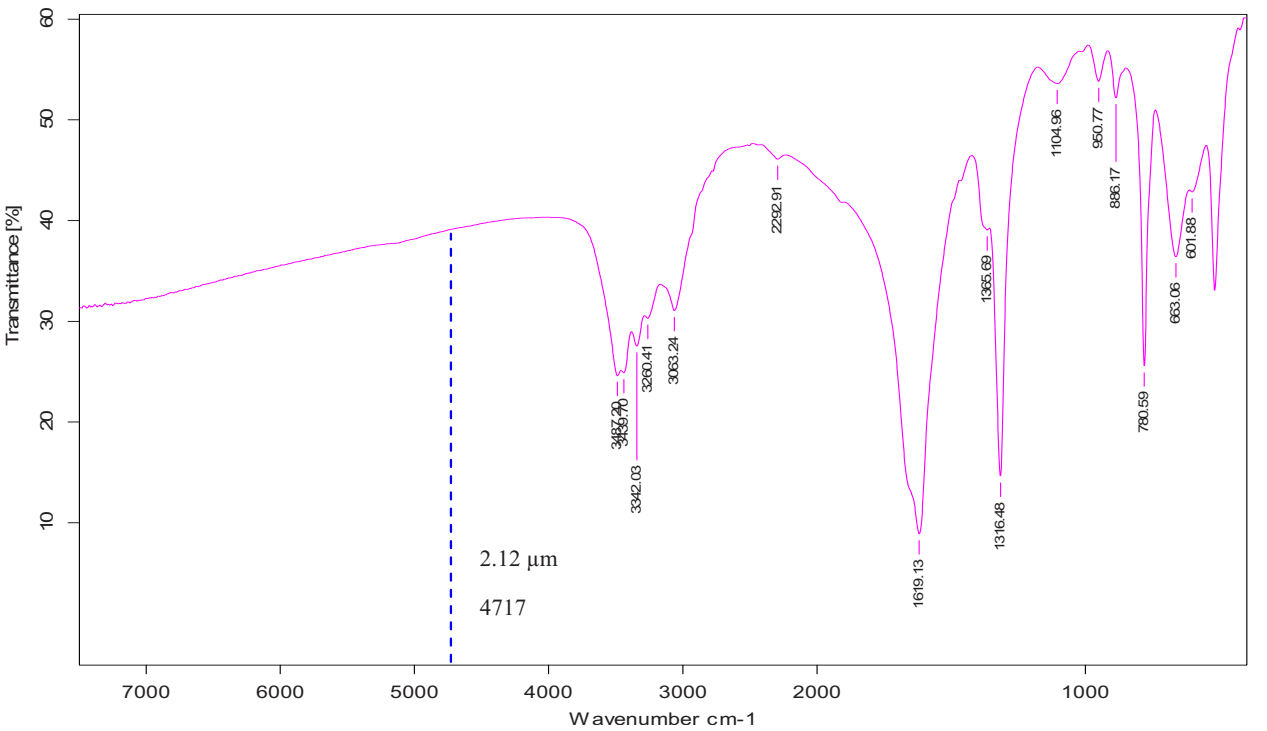

Fig. 3 Transmission of KBr-sample pellets for calculus with COM and UC constituents. COM is calcium oxalate monohydrate, and UC is uric acid.

application of adequate pressure for several minutes. We had to vary the KB_r and sample mix to get good transparency for a better signal-to-noise ratio and to obtain absorption bands strong enough to be detected at the same time. Figure 3 shows the Fourier-transform infrared transmission spectra of potassium bromide (KB_r)-sample pellets. This work has been finished at the Analytical and Testing Center, Huazhong University of Science and Technology. A 4717-cm^{-1} wavenumber corresponds to wavelength of 2.12 μm, as illustrated in Fig. 3.

2.3 *Ablation Valuation with Optical Coherent Microscopy System*

To obtain the quantitative ablation crater shape, an OCM system is used to measure quantitative ablation dimensions. The center wavelength is 650 nm and the bandwidth is 300 nm that provide axial and lateral resolutions of 2 μm with the 10× objective (NA=0.3). All cross sectional profiles that are at deepest position of the crater are displayed. The ablation volume can be estimated from OCM cross sections over the crater volume, and 3-D images are also given.

3 Results

3.1 *Bubble Dynamics*

To visualize the dynamics of the bubble formation at the distal fiber surface and in the underlying volume, high-speed photography was performed. The images for different core diameter (600, 400, and 200 μm, NA=0.22) fibers are shown in Figs. 4(a)–4(c), respectively. In Fig. 4(a), the bubble formation starts ~40 μs after laser start (ALS), and the bubble size reaches maximal value at 282 μs. At this time, the bubble has a characteristic pear shape and presents an excrescence (see arrow) on the wall opposite the fiber tip due to the continuing vaporization of water by the laser beam. At 454-μs ALS, the proximal part of the bubble is starting to collapse rapidly. Simultaneously, a cylindrical channel, due to further vaporization by the laser, is still progressing along the axis of the fiber tip. Finally, at 488-μs ALS, the complete collapse of the proximal bubble occurs with acoustic transient emission. The remnants (see arrow at 488 μs) of the channel collapse at 630 μs and the bubble size reaches the second minimal values. After that, the bubble undergoes the last oscillation with shorter oscillation periods observed by the naked eye. At 664 μs, the bubble size reaches the third maximal value again, and collapses completely at 684 μs. The results of Fig. 4(b) are similar to those of Fig. 4(a) in the starting phase, but a very interesting feature can be observed at 368 μs: the bubble shape is more like a cucurbit, because it can be divided into two distinct parts. The proximal part of the bubble, still quasispherical and centered on the fiber tip, is now collapsing rapidly. Simultaneously, a spheric channel, due to further vaporization by the laser, is still progressing along the axis of the fiber tip. Finally, at 668-μs ALS, the complete collapse of the proximal bubble occurs with acoustic transient emission. The remnants (see arrow at 556 μs) of the channel, only partially visible at the bottom of the pictures, experiences another oscillation. After 818 μs, the whole bubble disappears entirely. The results of Fig. 4(c) are also like those of Fig. 4(a), but the bubble shape is more irregular and we can only observe oscillation clearly twice due to small radiation energy of the fiber tip (only 22 mJ). The first and second maximal volumes (expand) occur at 270 and 716 μs (see arrows), respectively. The first and second collapse times occur at 444 and 842 μs, respectively. In some cases, even a third or fourth

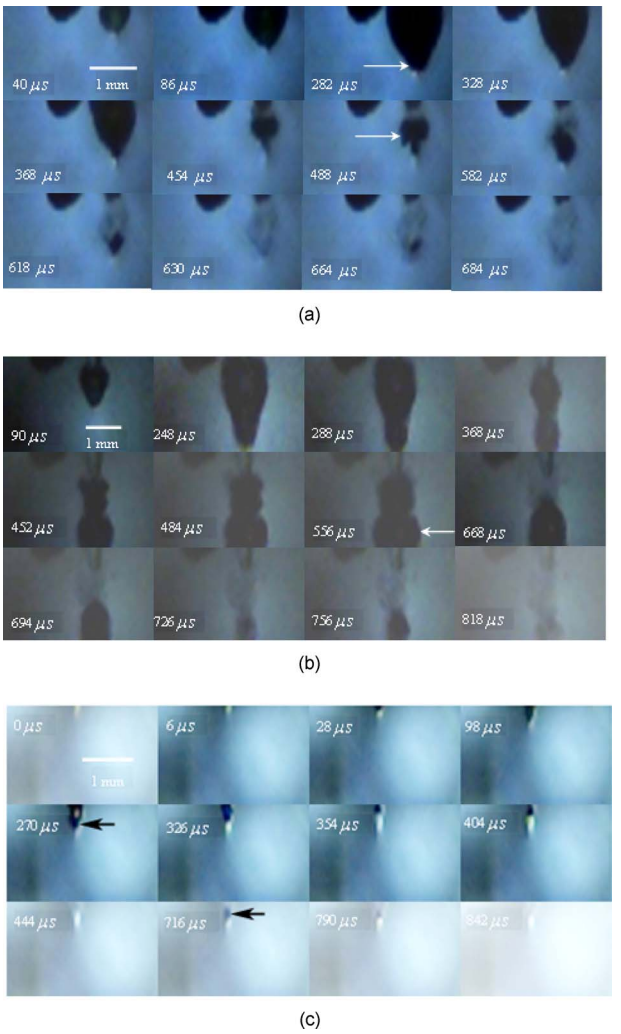

Fig. 4 Sequence of images of vapor bubble formation at the fiber tips with different cord diameters. (a) 600 μm, (b) 400 μm, and (c) 200 μm. The laser pulse duration is 300 μs and the laser pulse energy is 300, 240, and 22 mJ at the distal end of 600, 400, and 200-μm fibers, respectively. Times given are relative to the start of the laser pulse. A needle hydrophone is beside the 600-μm fiber in (a) and (b).

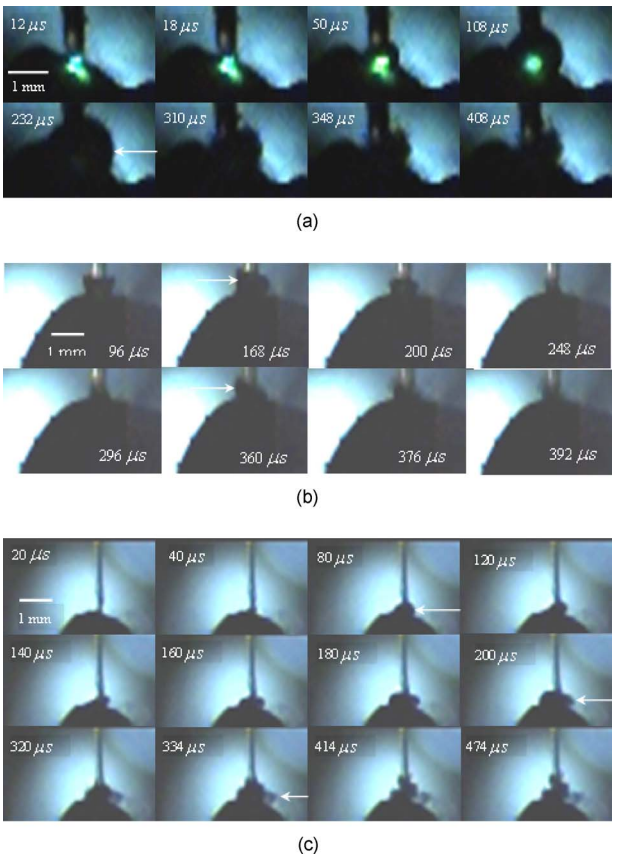

Fig. 5 Sequence of images of ablation products at the ends of different core diameter fibers: (a) 600, (b) 400, and (c) 200 μm. The laser pulse duration is 300 μs and the laser pulse energy is 300, 240, and 22 mJ at the distal end of 600, 400, and 200-μm fibers, respectively. Calculus with COM and UC constituents as hard tissue is ablated underwater. Times given are relative to the start of the laser pulse.

collapse generating an acoustic signal can be detected before the bubble finally dissolves into microbubbles. In these experiments, the high-speed camera is set at a speed rate of 500,000 frames per second with a spatial resolution of 256 $\times$16 pixels.

3.2 *Dynamics of Ablation Products*

In Fig. 5(a), a calculus with COM and UC constituents as hard tissue is ablated underwater, and the surface of it is not parallel with the 600-μm core diameter fiber tip. Actually, the right part of the free space (full of water) between them is bigger than that of the left. Consequently, the right ablation plume is bigger than the left ablation plume. At ~18-μs ALS, the ablation plume starts to occur and its size (see arrow) reaches a maximal value at 232 μs, and maintains a final size after 348 μs. To overcome the drawback of the uneven calculus surface, the fiber tip is in contact with the calculus surface, but there is still a little water between them, as illustrated in Fig. 5(b). At ~96-μs ALS, the ablation plume starts to grow and its size reaches maximal value (see arrow) at 168 μs. It reaches minimal value at 248 μs and the second smaller maximal value (see arrow) at 360 μs. Finally, at 392 μs it reaches the third minimal size of the ablation products and maintains at the same size after 392 μs. In Fig. 5(c), the ablation product volume undergoes three times oscillation because it reaches maximal values (see arrows) at 80, 200, and 334 μs, respectively. Accordingly, it reaches minimal values at 140, 300, and 414 μs, respectively, and maintains at the same value after 414 μs. The parameters of the high-speed camera for ablation experiments are set the same as those for cavitation effects (500,000 frames per second).

3.3 *Pressure Measurements*

Pressure transient occurrence and strength as a function of the delivering fiber diameter and laser fluence were studied. The laser-induced pressure waves generated at the submerged fiber tip were measured using a PVDF needle hydrophone. A high resistance termination on the pressure sensor yielded a signal amplitude that was proportional to the pressure. In our experiment, the absolute pressure waves were measured without a preamplifier. The diameter of the delivery fiber is an important parameter that influences pressure generation. At the

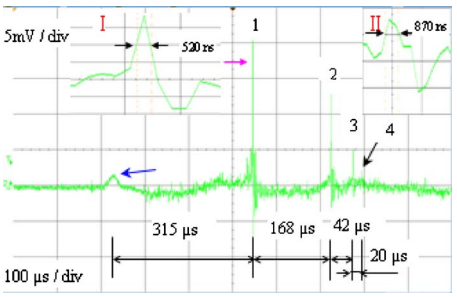

Fig. 6 Oscilloscope traces of the pressure transients induced by a single holmium pulse [E_p=300 mJ, 300 μs (FWHM), F_1=106 J/cm^2] at the submerged distal fiber tip(600-μm diameter). The increase in pressure (blue arrow) indicates the expansion of the generated bubble. The four pronounced pressure spikes after the end of a single holmium pulse are induced by the collapse of the bubble (1) and their rebounds (2, 3, and 4). Insert land II indicate the magnified pictures of the first and second pressure transients. (Color online only.)

same laser fluence, the diameter of the generated bubble scales with the fiber diameter. As smaller bubbles generate weaker pressure transients, the induced pressure amplitudes are significantly lower for smaller fiber diameters. On the other hand, for a given pulse energy delivered via different fibers, the induced pressure also generally decreases for decreasing fiber diameters. In this case, smaller fiber diameter means higher fluence regimes, which produce lower pressure amplitudes.[1]

To avoid repeating similar results, in this work the laser-induced pressure waves generated at the submerged fiber tip, only for the 600-μm core diameter fiber, are shown in Fig. 6. The pressure amplitudes are measured at 4-mm distance from the collapse center. The bubble formation starts at ~40-μs ALS in Fig. 4(a). A weak pressure increase 1.48 bar associated with the bubble expansion is observed. The first pressure wave is emitted with an amplitude of 20.3 bar 315 μs after bubble formation. Due to the laser pulse width of 300 μs, the first pressure wave induced by bubble collapse can be detected at 355-μs ALS. The second, third, and fourth pressure waves with amplitudes of 12.5, 5, and 2 bar at 4-mm distance from the collapse center, respectively, corresponding to the second, third, and fourth bubble collapse (after rebound), can be seen at intervals of 168, 42, and 20 μs as shown in Fig. 6.

3.4 *Comparision of Ablation Calculus in Air and Water*

The distinct difference between ablation in air and ablation in a liquid environment is that the liquid confines the movement of the ablation products. Therefore, ablation in a liquid environment is accompanied by bubble formation and by mechanical effects much stronger than those observed in a gaseous environment. This bubble is essential for the transmission of optical energy to the target, and the mechansims governing its formation and subsequent dynamics have thus received attention by various researchers.[10–15] In cases in which the fiber tip is placed in contact with the tissue surface, the ablation products are even more strongly confined than when they are surrounded by liquid alone. Furthermore, cavitation effects always occur during laser-tissue interaction processes in a liquid environment, even if the fiber tip is in contact with the tissue surface just because of a little liquid existing at the fiber tip in real conditions. For a given radiant exposure, the confining effect of the liquid or solid results in considerably higher temperatures and pressures within the target than ablation in a gaseous environment, because the expansion and adiabatic cooling of the ablation products proceed more slowly. Therefore, in a liquid environment, there is generally a more effective transduction of the laser energy into mechanical energy.[20]

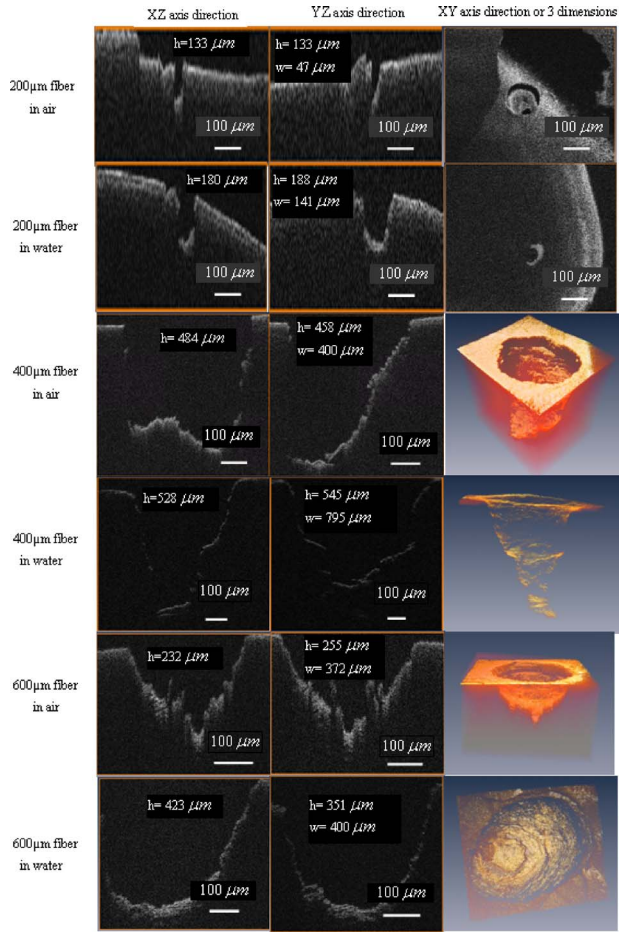

Fig. 7 Cross sectional topography of Ho:YAG laser-induced (ten successive lasers at a repetition rate of 1 Hz) craters acquired with the OCM system in air and water for different core diameter fibers. Note that *xy* direction cross-sectional topography is for only the 200-μm core diameter. The output intesnity per pulse at the fiber tips (200, 400, and 600 μm) can be averaged as 22, 240, and 300 mJ, respectively. h is height and w is width.

After exposure to ten consecutive holmium laser pulses at a repetition rate of 1 Hz in air and water, ablation craters of the calculus are scanned with an OCM instrument. The cross sectional profiles are displayed in Fig. 7. The cases can be mostly seen in actual clinical applications. To obtain the accurately quantitative ablation crater shape, an OCM system with lateral and axial resolutions of 2 μm was used to scan images from the *yz*, *xz*, and *xy* axes directions for the calculus irradiated by holmium laser transmitted in a 200-μm core diameter fiber, which are shown in the upper two rows, and *yz*, *xz*, and 3-D for 400 and 600-μm core diameter fibers are

shown in the following four rows. The height and width of the ablation craters are displayed in the corresponding images.

In our prior study, some conclusions can be drawn for laser ablation either in air or in water. 1. An increase in laser energy produces larger craters for all three fibers. 2. The crater shape is also affected by fiber size. At a given laser energy, irradiation with the larger fiber produces wider and shallower craters. 3. Ablation volume is a function of the fiber size and radiant exposure. 4. Even when the calculus surface is at an angle with respect to the laser beam, the ejected plume propagates in the direction normal to the calculus surface.[15,21–24] Therefore, in this work, to study the ablation difference in air and water, three series of ablation images for 200, 400, and 600-μm diameter fibers are presented in Fig. 7, respectively.

The crater diameters are always smaller than the fiber diameters used, and the crater diameters in air are smaller than those in water. But the first conclusion is not suitable for 400-μm core diameter fibers, because of the 400 and 795-μm crater diameters in air and water, shown in Fig. 7, are thought to be caused by calculus position shifting during the process of laser-calculus interaction. In addition, the crater height and ablation volume in air are always shorter and smaller than those in water, respectively. Finally, the important difference in the two cases is that the crater surface for underwater ablation is slippery, whereas that for in air is crude, as shown clearly in 3-D images in Fig. 7. In a word, for a certain core diameter fiber and pulse energy, ablation efficiency in water is higher than that in air.

4 Discussion

The purpose of this study was to visualize the dynamics of CBs and ablation products of hard tissue induced by a single holmium laser pusle transmitted in various core diameters of low OH^- fibers in water, and to evaluate the role of water layers during the process of tissue-laser interaction underwater by analyzing the tissue samples after laser ablation with an OCM system.

Our measurements show that CB created by free-running holmium lasers with pulse durations of 300 μs (FWHM) generate pressure transients of up to 20.3 bar at a distance of 4 mm from the collapse center. In that sense, holmium laser-induced CBs have a behavior during their collapse phase very similar to plasma-induced CBs generated by fs,[25–29] ps,[30,31] μs,[32,33] and ns (532 nm,[5,34–37] 1064 nm,[38–41] and 266 nm[42]) laser pulses. In particular, the characteristic bubble oscillation cycle with several subsequent collapses, rebounds, acoustic transient generations at the end of each collapse, and liquid jets are observed. However, contrary to the case of shorter laser pulse durations, the dynamcis of the bubble are strongly influenced by the long-lasting laser irradiation, which is continuous during bubble expansion. As the 2.12-μm laser radiation crosses the cavitation vapor without significant absorption, water is continuously evaporated at the bubble wall opposite the fiber tip. The radiant energy densities (F) at the distal fiber surface for the three different core diameters (200, 400, and 600 μm) are 70 J/cm^2, 190 J/cm^2, and 106 J/cm^2, respectively, which are all higher than the fluence threshold of 40 J/cm^2 for CB formation induced by holmium laser pulses underwater.[1] For the three series results via different fibers, the generated CB volume is directly concerned with the fiber diameter and the radiation energy density at the distal fiber surface, which will directly determine the pressure amplitudes.

Due to some liquid existing around the fiber surface, regardless of whether the fiber surface is in contact with the tissue surface or not in medical applications, a CB will form prior to laser-tissue interaction. Because the surfaces of the 600-μm fiber and calculus are not parallel to each other, F_1 = 106 J/cm^2 (600-μm fiber) is higher than F_3=70 J/cm^2 (200-μm fiber), so most of the pulse intensity is consumed for CB formation, but little can be used to ablate tissue. Consequently, in Fig. 5(a), at 232-μs ALS the plume reaches maximal size, which consists of water, gas, and calculus products. After that, some water and gas of the plume will disperse gradually, and finally the plume consists only of ablation calculus products. At 348-μs ALS, the plume size mainains a final value. However, unlike the 600-μm fiber, the process of a holmium laser with F_2=190 J/cm^2 for a 400-μm fiber irradiating calculus undergoes oscillation two times. Because the two surfaces are tightly in contact with each other, there is very little water between them. This case is similar to the case for the 200-μm fiber. Smaller laser intensity is consumed to induce CB formation. We can see clearly from Fig. 5(b) that, for the first oscillation, the ablation plume is composed of water and gas, but for the second oscillation, the ablation plume is composed of water, gas, and ablation products, because there are still calculus products after 392 μs. Similarly, the results for the 200-μm fiber is like those for the 400-μm fiber. However, there is still a difference for the two cases in that the latter process undergoes three oscillations even if F_3=70 J/cm^2 (200-μm fiber) is lower than F_2=190 J/cm^2 (400-μm fiber). For the last case, in Fig. 5(c), the first minimal plume volume (at 140 μs) is smaller than the second minimal plume volume (at 300 μs), and the second is also smaller than the third (at 414 μs). An interesting phenomenon is that the ablation products eject along the fiber axis directly during the third expand phase. After 414 μs, the ablation plume is clearly visible and maintains an invariable size. In a word, for the first case (600-μm fiber), one part of the laser pulse is consumed to induce bubble formation, and another part is used to irradiate the calculus. Finally, the oscillation time is only one and the ablation plume contracts because part of the bubble disperses after the maximal plume. For the second case (400-μm fiber), CB undergoes expansion and collapse without ablation calculus products during the first oscillation, but CB and ablation calculus occur during the second oscillation, which are induced by the other part of one laser pulse. For the third case (200-μm fiber), CB is accompanied by calculus products during all three oscillation phases. Evidently, the fiber end should not be a far distance from the tissue, or else most of the laser pulse will be consumed for cavitation effect and a small amout of pulse energy will be available for tissue ablation. Therefore, Pratisto et al.[43,44] used a holmium laser pulse as a prepulse to generate a CB, and during the bubble expanse phase erbium laser crosses the bubble and irradiates the tissue dirctly with minimal energy consumption.

Compared with other experimental results,[1,2,6,11–15,22] a gradual increase pressue signal (see blue arrow)[11] and subsequent four acoustic transients, as shown in Fig. 6, were de-

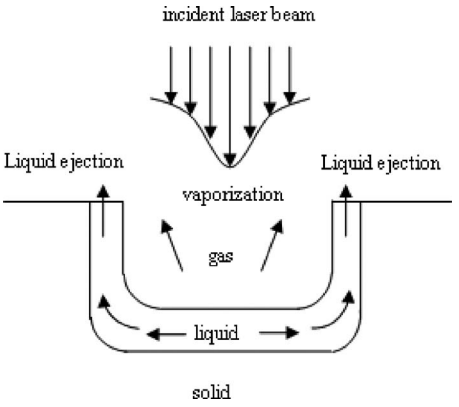

Fig. 8 Illustration of recoil-induced material expulsion.

tected by the hydrophone. This is the first time, to our knowledge, that up to four acoustic transients were detected under the condition of $F_1=106\ \mathrm{J/cm^2}$. The most obvious difference is that the bipolar shape of the four shock waves with a leading positive compression wave and a tailing negative wave was achieved in our experiemnt. However, both theoretical results[45–48] and the experimental results[1,2,6,11–15,22] of other researchers show there was only a leading positive compression wave. The corresponding magnification pictures for these four pressure waves are also achieved simultaneously. Due to limited space, only the prior two magnified pictures are presented in the left and right upper corners of Fig. 6. Their positive pulse widths (FWHM) are 520 and 870 ns, respectively, which can be easily seen. The two magnified pictures come from the oscillograph directly without any man-made changes. This phenomenon can be explained in terms of the conservation of momentum. If the cavitation threshold is exceeded but no material ejection takes places, the total momentum, which is proportional to the time integral over the stress wave, must remain zero. Therefore, the initial asymmetry of the bipolar wave has to be compensated by this additional negative stess.[45] Note that the response time (~several tens of nanoseconds) of the needle hydrophone might be too slow to detect the real-time shock wave signals accurately. Therefore, this phenomenon needs to be further explained theoretically and verified experimentally in our future work.

Enhancement of laser ablation in the presence of a liquid layer was verified by many researchers.[24,49–51] Moreover, Altshuler, Belikov, and Sinelnik[52] have proposed that solid particles of ablated material are accelerated against the walls of the crater, resulting in a polishing effect that removes debris and any protruding sharp edges. Based on this hypothesis, a similar crater surface will be expected both in air and in water, but the results are contrary. The difference attributes to a recoil-induced material expulsion effect and flow-induced material redeposition during the ablation process in water.[53] Variations of the recoil stress amplitude in the radial direction result in a force driving the water toward the edges of the ablation crater and out of the crater, as illustrated schematically in Fig. 8.[53] The recoil stress produced by both vaporization and material ejection through explosion and confined boiling can induce a secondary material expulsion process that decreases the shielding effect and provides a strong increase of the ablation efficiency.[53] Additionally, due to a holmium laser pulse consisting of multispikes (nanosecond width), every laser spike can satisfy the stress confinement condition and induce a bipolar acoustic wave. A negative wave of a bipolar wave can decrease the ablation threshold of tissue, because tissue is more susceptible to damage from tensile and shear stresses than to compressive stress.[54,55]

A nondestructive method to quantitatively measure hard tissue irradiated by laser pulses was conventionally based on an OCT system ($\lambda_0=1290$ nm, $\Delta\lambda=42$ nm, and P $=2.2$ mW) with lateral and axial resolutions of 20 μm.[15,22–24,56] In our work, an OCM system was used to measure quantitative ablation dimensions (the center wavelength is 650 nm and the bandwidth is 300 nm) that provided axial and lateral resolutions of 2 μm with a 10× objective (NA=0.3). Every cross sectional profile at the deepest positions of the crater are displayed. The ablation volume can be estimated from OCM cross sections over the crater volume, and the 3-D images are also given. Our measurements for calculus craters using the OCM system is higher by one order than those using the OCT system, which helps us evaluate the role of water during the process of laser-tissue interaction by analyzing crater shape and volume accurately.

5 Conclusions

In this work the complete dynamics of CBs, ablation products, and acoustic transients, which are all induced by a single 300-μs (FWHM) holmium laser pulse transmitted in different core diameter (200, 400, and 600 μm) fibers, are recorded and detected by means of high-speed photography and an acoustic pressure sensor, respectively. Maximal CB volume is related directly to both the laser pulse energy and fiber diameter, which further determines the acoustic pressure amplitudes. This indicates a possible cause of acoustical tissue damage during medical applications in a liquid environment, as in arthroscopic or angioplastic surgery. By analyzing the pictures taken by high-speed camera and scaned by the OCM system, it is easily seen that the liquid layer plays an important role during the process of laser-tissue interaction, which can increase ablation efficiency, decrease heat side effects, and reduce cost.

Acknowledgments

The project was supported by the Special Fund for Basic Scientific Research of Central Colleges, China University of Geosciences (Wuhan) (CUG090112).

References

1. T. Asshauer, K. Rink, and G. Delacretaz, "Acoustic transient generation by holmium-laser-induced cavitation bubbles," *J. Appl. Phys.* **76**, 5007–5013 (1994).
2. O. Fohn, H. S. Pratisto, F. Konz, M. Ith, H. J. Altermatt, M. Frenz, and H. P. Weber, "Side-firing fiber device for underwater tissue ablation with Ho:YAG and Er:YAG laser radiation," *J. Biomed. Opt.* **3**(1), 112–122 (1998).
3. G. S. Fanton and M. F. Dillingham, "The use of the holmium:YAG-laser in arthroscopic surgery," *Semin. Orthop.* **7**, 102–116 (1992).
4. M. Ith, H. Pratisto, H. U. Staubli, H. J. Altermatt, M. Frenz, and H. P. Weber, "Side effects of laser therapy on cartilage," *Sports Exercise Injury* **2**, 207–209 (1996).
5. A. B. Karpiouk, S. R. Aglyamov, F. Bourgeois, A. Ben-Yakar, and S. Y. Emelianov, "Quantitative ultrasound method to detect and monitor laser-induced cavitation bubbles," *J. Biomed. Opt.* **13**(3), 034011 (2008).

6. M. Frenz, G. Paltauf, and H. Schmidt-kloiber, "Laser-generated cavitation in absorbing liquid induced by acoustic diffraction," *Phys. Rev. Lett.* **76**, 3546–3549 (1996).
7. R. Brinkmann, C. Hansen, D. Mohrenstecher, M. Scheu, and R. Birngruber, "Analysis of cavitation dynamics during pulsed laser tissue ablation by optical on-line monitoring," *IEEE J. Quantum Electron.* **2**, 826–835 (1996).
8. E. A. Brujan, K. Nahen, P. Schmidt, and A. Vogel, "Dynamics of laser-induced cavitation bubbles near an elastic boundary," *J. Fluid Mech.* **433**, 251–281 (2001).
9. E. A. Brujan, K. Nahen, P. Schmidt, and A. Vogel, "Dynamics of laser-induced cavitation bubbles near elastic boundaries: influence of the elastic modulus," *J. Fluid Mech.* **433**, 283–314 (2001).
10. W. Wagner, A. Sokolow, R. Peartstein, and G. Edwards, "Thermal vapor bubble and pressure dynamics during infrared laser ablation of tissue," *Appl. Phys. Lett.* **94**, 013901 (2009).
11. M. Frenz, F. Konz, H. Pratisto, and H. P. Weber, "Starting mechanisms and dynamics of bubble formation induced by a Ho:YAG aluminum garnet laser in water," *J. Appl. Phys.* **84**, 5905–5912 (1998).
12. M. Frenz, H. Pratisto, F. Konz, E. D. Jansen, A. J. Welch, and H. P. Weber, "Comparison of the effects of absorption coefficient and pulse duration of 2.12-μm and 2.79-μm radiation on laser ablation of tissue," *IEEE J. Quantum Electron.* **32**, 2025–2035 (1996).
13. T. Asshauer, G. Delacretaz, E. D. Jansen, A. J. Welch, and M. Frenz, "Pulsed holmium laser ablation of tissue phantoms: correlation between bubble formation and acoustic transients," *Appl. Phys. B* **65**, 647–657 (1997).
14. E. D. Jansen, T. Asshauer, M. Frenz, M. Motamedi, G. Delacretaz, and A. J. Welch, "Effect of pulse duration on bubble formation and laser-induced pressure waves during Holmium laser ablation," *Lasers Surg. Med.* **18**, 278–293 (1996).
15. H. W. Kang, H. Lee, J. M. H. Teichman, J. Oh, J. Kim, and A. J. Welch, "Dependence of calculus retropulsion on pulse duration during Ho:YAG laser lithotripsy," *Lasers Surg. Med.* **38**, 762–772 (2006).
16. E. A. Brujan and A. Vogel, "Stress wave emission and cavitation bubble dynamics by nanosecond optical breakdown in a tissue phantom," *J. Fluid Mech.* **558**, 281–308 (2006).
17. Y. Tomita and T. Kodama, "Interaction of laser-induced cavitation bubbles with composite surfaces," *J. Appl. Phys.* **94**, 2809–2816 (2003).
18. G. N. Sankin, W. N. Simmons, S. L. Zhu, and P. Zhong, "Shock wave interaction with laser-generated single bubbles," *Phys. Rev. Lett.* **95**, 034501 (2005).
19. D. Obreschkow, P. Kobel, N. Dorsaz, A. de. Bosset, C. Nicollier, and M. Farhat, "Cavitation bubble dynamics inside liquid drops in microgravity," *Phys. Rev. Lett.* **97**, 094502 (2006).
20. A. Vogel, J. Noack, K. Nahen, D. Theisen, S. Busch, U. Parlitz, D. X. Hammer, G. D. Noojin, B. A. Rockwell, and R. Birngruber, "Energy balance of optical breakdown in water at nanosecond to femtosecond time scales," *Appl. Phys. B* **68**, 271–280 (1999).
21. K. F. Chan, G. J. Vassar, T. J. Pfefer, J. M. H. Teichman, R. D. Glickman, S. T. Weintraub, and A. J. Welch, "Holmium:YAG laser lithotripsy: a dominant photothermal ablative mechanism with chemical decomposition of urinary calculi," *Lasers Surg. Med.* **25**, 22–37 (1999).
22. H. Lee, R. T. Ryan, J. Kim, B. Choi, N. V. Arakeri, J. M. H. Teichman, and A. J. Welch, "Dependence of calculus retropulsion dynamics on fiber size and radiant exposure during Ho:YAG lithotripsy," *J. Biomech. Eng.* **126**, 506–515 (2004).
23. H. Lee, H. W. Kang, J. M. H. Teichman, J. Oh, and A. J. Welch, "Urinary calculus fragmentation during Ho:YAG and Er:YAG lithotripsy," *Lasers Surg. Med.* **38**, 39–51 (2006).
24. H. W. Kang and A. J. Welch, "Effect of liquid thickness on laser ablation efficiency," *J. Appl. Phys.* **101**, 083101 (2007).
25. J. Noack, D. X. Hammer, G. D. Noojin, B. A. Rockwell, and A. Vogel, "Influence of pulse duration on mechanical effects after laser-induced breakdown in water," *J. Appl. Phys.* **83**, 7488–7495 (1998).
26. S. R. Aglyamov, A. B. Karpiouk, F. Bourgeois, A. B. Yakar, and S. Y. Emelianov, "Ultrasound measurements of cavitation bubble radius for femtosecond laser-induced breakdown in water," *Opt. Lett.* **33**, 1357–1359 (2008).
27. W. Kautek, J. Kruger, M. Lenzner, S. Sartania, C. Spielmann, and F. Krausz, "Laser ablation of dielectrics with pulse duration between 20 fs abd 3 ps," *Appl. Phys. Lett.* **69**, 3146–3148 (1996).
28. B. M. Kim, A. M. Komashko, A. M. Rubenchik, M. D. Feit, S. Reid, and L. B. D. Silva, "Interferometric analysis of ultrashort pulse laser-induced pressure waves in water," *J. Appl. Phys.* **94**, 709–715 (2003).
29. E. N. Glezer, C. B. Schaffer, N. Nishimura, and E. Mazur, "Minimally disruptive laser-induced breakdown in water," *Opt. Lett.* **22**, 1817–1819 (1997).
30. B. Zysset, J. G. Fujimoto, and T. F. Deutsch, "Time-resolved measurements of picosecond optical breakdown," *Appl. Phys. B* **48**, 139–147 (1989).
31. A. Vogel and S. Busch, "Shock wave emission and cavitation bubble generation by picosecond and nanosecond optical breakdown in water," *J. Acoust. Soc. Am.* **100**, 148–165 (1996).
32. K. Rink, G. Delacretaz, and R. P. Salathe, "Fragmentation process induced by microsecond laser pulses during lithotripsy," *Appl. Phys. Lett.* **61**, 258–260 (1992).
33. H. Q. Shangguan, L. W. Casperson, and S. A. Prahl, "Pressure impulses during microsecond laser ablation," *Appl. Opt.* **36**, 9034–9041 (1997).
34. D. Lapotko, "Optical excitation and detection of vapor bubbles around plasmonic nanoparticles," *Opt. Express* **17**, 2538–2556 (2009).
35. P. A. Quinto-Su, V. Venugopalan, and C. D. Ohl, "Generation of laser-induced cavitation bubbles with a digital hologram," *Opt. Express* **16**, 18964–18969 (2008).
36. K. Y. Lim, P. A. Q. Su, E. Klaseboer, B. C. Khoo, V. Venugopalan, and C. D. Ohl, "Nonspherical laser-induced cavitation bubbles," *Phys. Rev. E* **81**, 016308 (2010).
37. R. Evans, S. C. Lopez, F. G. P. Gutierrez, and G. Aguilar, "Pump-probe imaging of nanosecond laser-induced bubbles in agar gel," *Opt. Express* **16**, 7481–7492 (2008).
38. L. Martí-López, R. Ocaña, J. A. Porro, M. Morales, and J. L. Ocaña, "Optical observation of shock waves and cavitation bubbles in high intensity laser-induced shock processes," *Appl. Opt.* **48**, 3671–3680 (2009).
39. R. Petkovsek and J. Mozina, "Optodynamics characterization of the shock waves after laser-induced breakdown in water," *Opt. Express* **13**, 4107–4112 (2005).
40. R. Petkovsek and P. Gregorcic, "A laser probe measurement of cavitation bubble dynamics improved by shock wave detection and compared to shadow photography," *J. Appl. Phys.* **102**, 044909 (2007).
41. P. Gregorčič, R. Petkovšek, J. Možina, and G. Močnik, "Measurements of cavitation bubble dynamics based on a beam-deflection probe," *Appl. Phys. A* **93**, 901–905 (2008).
42. X. Zeng, X. Mao, S. S. Mao, S. B. Wen, R. Greif, and R. E. Russo, "Laser-induced shockwave propagation from ablation in a cavity," *Appl. Phys. Lett.* **88**, 061502 (2006).
43. H. Pratisto, M. Ith, M. Frenz, and H. P. Weber, "Infrared multiwavelength laser system for establishing a surgical delivery path through water," *Appl. Phys. Lett.* **67**, 1963–1965 (1995).
44. H. Pratisto, M. Frenz, M. Ith, H. J. Altermatt, E. D. Jansen, and H. P. Weber, "Combination of ifber-guided pulsed erbium and holmium laser radiation for tissue ablation under water," *Appl. Opt.* **35**, 3328–3337 (1996).
45. G. Paltauf and H. S. Kloiber, "Microcavity dynamics during laser-induced spallation of liquids and gels," *Appl. Phys. A* **62**, 303–311 (1996).
46. G. Paltauf and H. S. Kloiber, "Photoacoustic waves excited in liquids by fiber-transmitted laser pulses," *J. Acoust. Soc. Am.* **104**, 890–897 (1998).
47. G. Paltauf and H. S. Kloiber, "Photoacoustic cavitation in spherical and cylindrical absorbers," *Appl. Phys. A* **68**, 525–531 (1999).
48. E. A. Brujan, "Dynamics of shock waves and cavitation bubbles in bilinear elastic-plastic media, and the implications to short-pulsed laser surgery," *Eur. Phys. J.: Appl. Phys.* **29**, 115–123 (2005).
49. H. W. Kang, H. Lee, and A. J. Welch, "Laser ablation in a liquid-confined environment using a nanosecond laser pulse," *J. Appl. Phys.* **103**, 083101 (2008).
50. S. Zhu, Y. F. Lu, and M. H. Hong, "Laser ablation of solid substrates in a water-confined environment," *Appl. Phys. Lett.* **79**, 1396–1398 (2001).
51. S. Zhu, Y. F. Lu, and X. Y. Chen, "Laser ablation of solid substrates in water and ambient air," *J. Appl. Phys.* **89**, 2400–2403 (2001).
52. G. B. Altshuler, A. V. Belikov, and Y. A. Sinelnik, "A laser-abrasive method for the cutting of enamel and dentin," *Lasers Surg. Med.* **28**, 435–444 (2001).

53. A. Vogel and V. Venugopalan, "Mechanisms of pulsed laser ablation of biological tissues," *Chem. Rev.* **103**, 577–644 (2003).
54. A. D. Zweig, "A thermo-mechanical model for laser ablation," *J. Appl. Phys.* **70**, 1684–1691 (1991).
55. D. Albagli, M. Dark, L. T. Perelman, C. V. Rosenberg, I. Itzkan, and M. S. Feld, "Photomechanical basis of laser ablation of biological tissue," *Opt. Lett.* **19**, 1684–1686 (1994).
56. H. W. Kang, H. Lee, S. Chen, and A. J. Welch, "Enhancement of bovine bone ablation assisted by a transparent liquid layer on a target surface," *IEEE J. Quantum Electron.* **42**, 633–642 (2006).